PHOTONICS Research

Microfluidic integrated metamaterials for active terahertz photonics

Zhang Zhang,[1,†] Ju Gao,[2,3] Maosheng Yang,[4,†] Xin Yan,[2] Yuying Lu,[1] Liang Wu,[1] Jining Li,[1] Dequan Wei,[2] Longhai Liu,[5] Jianhua Xie,[5] Lanju Liang,[1,2,*] and Jianquan Yao[1,6]

[1]Key Laboratory of Opto-Electronics Information Technology, Institute of Laser and Opto-Electronics, College of Precision Instruments and Opto-Electronics Engineering, Tianjin University, Tianjin 300072, China
[2]School of Opto-Electronic Engineering, Zaozhuang University, Zaozhuang 277160, China
[3]Department of Physics, The University of Hong Kong, Hong Kong, China
[4]School of Mechanical Engineering, Jiangsu University, Zhenjiang 212013, China
[5]Advantest (China) Co., Ltd., Shanghai 201203, China
[6]e-mail: jqyao@tju.edu.cn
*Corresponding author: lianglanju123@163.com

Received 8 August 2019; revised 15 September 2019; accepted 2 October 2019; posted 4 October 2019 (Doc. ID 374956); published 15 November 2019

A depletion layer played by aqueous organic liquids flowing in a platform of microfluidic integrated metamaterials is experimentally used to actively modulate terahertz (THz) waves. The polar configuration of water molecules in a depletion layer gives rise to a damping of THz waves. The parallel coupling of the damping effect induced by a depletion layer with the resonant response by metamaterials leads to an excellent modulation depth approaching 90% in intensity and a great difference over 210° in phase shift. Also, a tunability of slow-light effect is displayed. Joint time-frequency analysis performed by the continuous wavelet transforms reveals the consumed energy with varying water content, indicating a smaller moment of inertia related to a shortened relaxation time of the depletion layer. This work, as part of THz aqueous photonics, diametrically highlights the availability of water in THz devices, paving an alternative way of studying THz wave–liquid interactions and developing active THz photonics.

https://doi.org/10.1364/PRJ.7.001400

1. INTRODUCTION

Electromagnetic metamaterials (MMs) [1], consisting of periodically arranged subwavelength "meta-atoms" as building blocks, can resonate with incident electromagnetic waves. Hence, it gives an opportunity to break through the limitation in traditional fields due to the extraordinary properties that are not achievable in natural materials. The well-known basic block is split-ring resonators (SRRs) [2]. Based on different shapes, sizes, and arrangements of SRRs, the optical property of MMs can be "designed" in desirable ways [3], which brings unprecedented developments in communication [4], sensing [5,6], and hologram imaging [7,8]. However, the fixed structures of SRRs make such "designs" imperfect owing to the unalterable resonant characteristic, weakening their control of the electromagnetic waves in a larger degree of freedom. Although there are some reconfigurable SRRs for dynamic modulation reported [9], the inefficient modulation property still needs to be improved. To overcome the problem, various tunable methods have been proposed and extensively studied in optical and microwave bands [10–15]. The terahertz (THz) wave is attracting great attention in the research community because of its unique properties such as being broadband, nondestructive, and transparent for most dielectrics [16,17]. Emphasizing the operating frequency that locates in the THz range, the MMs are of importance for the active modulation of THz waves. A frequently employed method in the THz range is exerting an optical or electrical field. Either of the fields may serve as external "tuning-button" of MMs to modulate THz waves with the advantages of shorter recovery time (tens of picoseconds) and easier implementation of excitation source compared with others [18–23]. Generally, both techniques require the tunable external fields (light irradiation or gating voltage) and the formation of heterostructures by hybridizing meta-atoms with active media such as semiconductors [18,20], perovskites [19], graphene [22,23], and other media [21]. Thereby, the resultant electron excitation in the medium induced by field effects gives rise to the changing electronic property of heterostructures, whose controllable dielectric properties offer access to tuning the amplitude, resonant frequency, and phase shift of THz waves. Nevertheless, in the two schemes, some problems should be taken into account. First of all, an extra light or electrical source to stimulate the corresponding medium needs to be

supplemented properly in the measuring systems. Yet, after the system preparation, the induced photothermal effect or electric breakdown of medium is still at the risk of disabling the metadevices probably caused by the strong optical illumination or large electric voltage. Second, the charge transfer in the heterostructures is more likely a "chain reaction." Once the complicated fabrication produces the defective interface and degraded material characteristics that largely influence the charge transfer [24], the poor performance of heterostructures would lead to practical difficulties in realizing a stable tunability of THz waves. Considering the above disadvantages, it is necessary to develop a completely different strategy of active modulation without the excitation of external fields and the fabrication of heterostructures. To reach this goal, finding a material that can independently interact with THz waves and conveniently assemble with meta-atoms turns out to be the key.

Water, one of the most common materials in nature, may become an alternatively favorable candidate. Unlike the charge–excitation mechanism in the aforementioned medium, the polar configuration of water molecules would result in the damping of THz waves due to strong absorption. Therefore, in a sense, such a damping effect should be minimized in measuring systems in order to gain a high intensity of THz waves. However, by conversely utilizing water as a medium thanks to its independent damping of THz waves, it may give rise to an external-source free technique to modulate THz waves by coupling such a damping effect on the resonating of metadevices, simultaneously providing that the damping effect induced by water can be tuned in it. For this purpose, the microfluidics are well qualified. Numerous applications of microfluidics in biological and medical fields have been demonstrated [25]. Recent attempts to incorporate photonic components into microfluidic devices expand the functionality and the frontier of traditional optics [26]. By exploiting the microfluidics to couple the depletion layer with MMs and to tune the damping effect of water, the actively modulated THz waves can be highly expected.

Here, we engineer a depletion layer served by the aqueous organic liquids that are flowing in a specifically designed platform of microfluidic integrated metamaterials (MIMs). To actively modulate the characteristics of THz waves, the damping effect of the depletion layer was tuned by injecting a small amount of water in organic liquids flowing in MIMs through a mechanical micropumping system. A gradual reduction of transmission and a shift of resonant peaks with the increasing water content in MIMs are observed in the experiments and match the simulation very well. The results can be attributed to the weakened localized field strength and the changed mode coupling of SRRs, which is revealed by field analysis and the theoretical model. The wavelet transform gives an insight into the damping effect induced by water in MIMs. With the increasing of water content from 0% to 100%, the enhancement of extinction and the shortened time duration between the two interaction positions imply a greater energy loss of THz waves and a smaller moment of inertia of water molecules, respectively. The latter offers opportunities to establish a fast modulation process. By choosing different aqueous organic liquids, the modulated transmission intensity and phase shift of THz waves are realized in the MIMs platform. The acetone exhibits the maximum modulation depth in transmission intensity close to 90%, whereas the largest phase difference (over 210°) presents in isopropyl alcohol (IPA). This work diametrically highlights the availability of water in THz devices, opening up a new window for active THz photonics with various advantages, including flexible liquid choice, replaceable meta-atoms, nondestructive measurements, and no external field stimulation.

2. EXPERIMENTAL MEASUREMENT AND SIMULATION MODEL

Figure 1(a) shows the whole structure of the designed platform. The incident E_y-polarized THz waves penetrate the MIMs, in which the liquid flows from the inlet to the outlet port at a certain speed under control of the micropumping system, seen in Fig. 2. By adjusting different flow speeds in different channels in the multichannel micropumping system, the mixture ratio of liquids flowing through MIMs would be modulated continuously. To give a clear illustration, the trilayer device is decomposed layer by layer [Fig. 1(b)]. The bottom quartz (500 μm in thickness) serves as substrate to support the patterned SRRs array that is acquired by standard photolithography followed by the deposition of a titanium layer of 20 nm and an aluminum layer of 200 nm. The corresponding optical microscopy image of SRRs is shown in Fig. 1(d). All dimensional parameters of the designed SRRs [Fig. 1(e)] are denoted

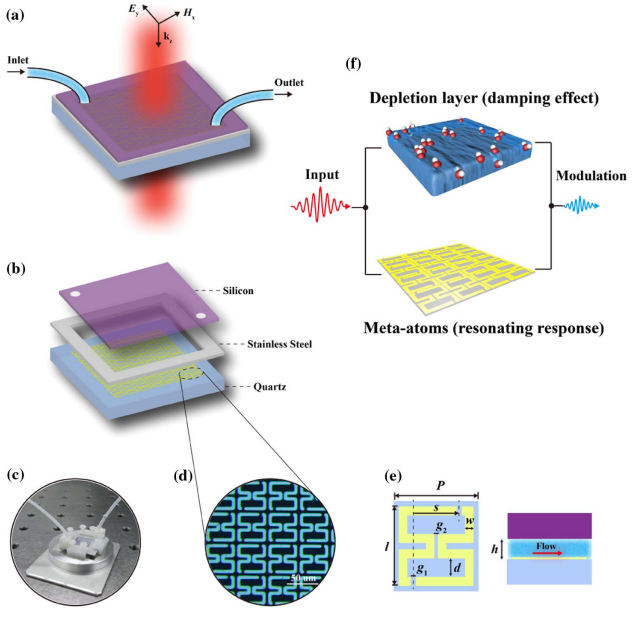

Fig. 1. (a) Schematic of MIMs platform with liquid flowing through from the inlet to the outlet under the irradiation of E_y-polarized THz waves; (b) tri-layer structure of the MIMs platform; (c) photograph of real MIMs device; the clamp and screws are used to package the layer materials and the soft pipes to guide the fluids. (d) Optical microscopy image of fabricated SRRs in a certain region; (e) geometric configuration of SRRs; all of the structural parameters are $P = 48$ μm, $l = 44$ μm, $w = 5$ μm, $d = 10.25$ μm, $g_1 = 3$ μm, $g_2 = 2$ μm, $s = 27$ μm, and $h = 35$ μm. (f) Schematic illustration of parallel modulation mechanism.

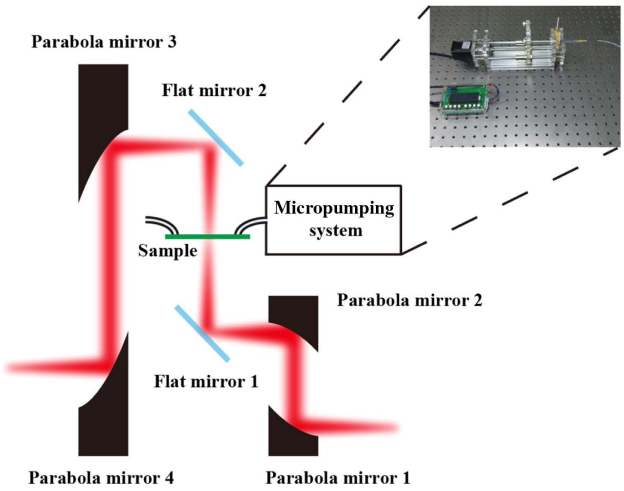

Fig. 2. Schematic of THz–TDS measurement system. Photograph of micropumping system is shown as inset.

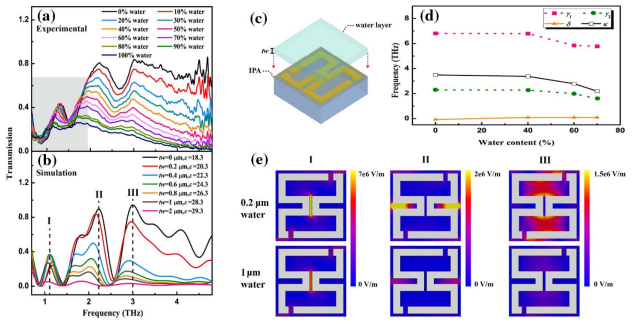

Fig. 3. (a) Measured THz transmission spectra for the MIMs sample showing the modulation of resonant peaks with varying water content from 0% to 100%; (b) corresponding simulation spectra, whereby the increasing water content levels are represented by an increasing water-layer thickness together with the enhancement of IPA-layer permittivity. (c) Schematic illustration of simulated model, in which the water layer and IPA layer are created to simulate the water effect in reality; (d) parameters extracted from the coupled Lorentz oscillator model by fitting the experiments in the frequency range marked as gray in (a) under different water contents; (e) electric field monitored to SRRs under 0.2 and 2 μm water-layer thickness at three resonant peaks marked as I, II, and III in (b), respectively.

and given in the caption. The 500-μm-thick silicon is selected as a capping layer with two holes to let the liquids flow in and flow out. Between the capping and bottom layer, a frame of stainless steel 35 μm in thickness is inserted to form the microfluidic space. All layers with the size of 1 cm × 1 cm are packaged together by screws, and the liquids are conducted into MIMs through soft pipes, as shown in Fig. 1(c). Notably, Fig. 1(f) schematically illustrates the mechanism of parallel modulation, which is realized by coupling the damping effect of the depletion layer with the resonating response of metadevices. In contrast with the serial transfer manner of charges in common heterostructures, the damping effect of the liquid depletion layer and the resonating response of MMs are independent in our MIMs. Such a parallel coupling mechanism enables us to desirably tune the water content of aqueous organic liquids in the depletion layer and to replace the meta-atoms with others in the MM layer, performing the active modulation with good performance and in a much more flexible manner.

In order to tune the damping effect of the depletion layer by controlling the water content in the microfluidic system, the organic liquids are adopted as the background matrix (which would be deducted in experiments) to carry water molecules. By changing the mixing ratio of water in the background matrix, the MIMs platform exhibits a tunable transmission. Figure 3(a) shows the experimental transmission under different water contents in IPA liquid flowing through MIMs at the rate of 0.25 mL/h. To consider only the effect of water on the MMs resonance, the measured spectra of MIMs are normalized by that of the reference sample, which is made on a bare quartz substrate without SRRs and is measured under a fluid of 100% IPA at the same speed. The results show that, with the increasing water content, the transmission is well modulated mainly at three peak positions caused by MMs: the Fano peak I at 1.18 THz decreasing from 37% to 21%, the Fano peak II at 2.21 THz from 80% to 20%, and the hybrid mode peak at 3.01 THz (as labeled III) from 84% to 14%. Except for the reduction of transmission intensity, the position of peak II also presents a larger redshift of 0.46 THz in frequency compared with that of other peaks. The intensity reduction of THz waves may be attributed to the enhanced damping effect due to a larger absorption by water. Meanwhile, the change of average permittivity induced by water could affect the near-field coupling of SRRs, which gives rise to the shift of resonant peaks. Both effects caused by water can be numerically simulated by finite-difference time-domain computation using CST Microwave Studio software. Owing to the complicated physical nature of the water–IPA mixture, for convenience, the influence resulting from water is simplified into two independent parts in simulation: the damping effect and the varying average permittivity. For the former, a water layer with a different thickness t_w changing from 0 to 2 μm is built. Because the liquids are flowing on the surface of the MMs in the MIMs system, the MMs were taken as the bottom layer. On the other hand, the organic liquids were adopted as the background matrix to carry water molecules in our experiments. Therefore, there are a much larger number of IPA molecules than water molecules. In other words, in the near field of MMs, the IPA layer should have a stronger effect than the water layer. Thus, the IPA layer was added on the surface of the MM, and the water layer was placed above the IPA layer to simulate the depletion layer. Additionally, in order to separate the damping effect from the near-field coupling, a spacing between the water layer and MMs surface is created. Because the thickness parameter has little influence on the whole model explanation in simulation, a moderate spacing thickness of 20 μm is selected [shown in Fig. 3(c)]. As for the varying average permittivity, since the permittivity of pure IPA (~18.3) is much less than that of water [27], another layer of 0.4 μm with permittivity ε from 18.3 to 29.3 was added on the SRRs' surface to make an effective interaction in near fields. We measured the dielectric parameter of quartz used in simulation and imported it into software for calculation. The electric and magnetic boundary conditions are selected to simulate the E_y-polarized plane waves that normally

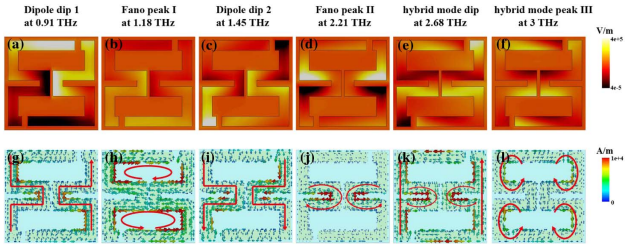

Fig. 4. (a)–(f) Electric field distribution of SRRs at 0.91, 1.18, 1.45, 2.21, 2.68, and 3 THz, respectively. (g)–(l) The corresponding surface currents density of SRRs at different frequencies; the red arrows represent the currents' flowing direction.

impinge on MMs structures. As illustrated in Fig. 3(b), the simulation results similarly match with the corresponding experimental ones except for a little difference in peak location at peak I. A possible explanation is that the electromagnetic response influenced by such an inconsistent permittivity between the simulation and experiment may mainly reflect the resonance at lower frequencies, thus making a location difference at the position of peak I. Additionally, the real silicon material used in experiment may also induce such a simulation–experiment difference due to the defect introduction.

In order to give a detailed analysis on resonant mechanism at each position, the corresponding localized electric field distribution and surface currents density are monitored in simulation and shown in Fig. 4. At 0.91 THz, the polarized electric field and single direction of currents distributed on the two sides of the SRRs imply the typical dipole resonant mode (bright mode); thereby the strong radiative loss is generated and leads to an obvious transmission dip. With the increasing of frequency to 1.18 THz, it is found that two circulating currents appear in the upper and bottom metal rings. Such circulating currents induce magnetic resonance with low radiative loss (dark mode) in the two metal rings, which couples with the bright mode generated at the lower frequency. Therefore, the destructive interference between the bright and dark mode happens and gives rise to the suppression of the bright mode. As a result, the strength of the electric field is reduced and the transmission improves to a peak. Similarly, when the frequency reaches 1.45 THz, the dipole mode emerges again; the only difference compared with dip 1 is that the currents' flowing direction is reversed. After the frequency arrives at 2.21 THz, unlike the Fano peak I, the circulating currents appear on the left and right middle of the SRRs under this condition. Also, the destructive interference resulting from the coupling of the bright and dark modes suppresses the radiative loss and gives the second peak, labeled Fano peak II. Subsequently, the hybrid resonant mode is acquired when the frequency is at 2.68 THz; except for the circulating currents in the middle of the SRRs, the dipole resonant mode coexists on the two straight sides of the SRRs. In this case, the transmission decreases due to the enhanced radiative loss caused by dipole resonance. Eventually, with the frequency increasing to 3 THz, the circulating currents are formed at the four corners of SRRs simultaneously; the induced magnetic resonance would destructively interfere with the dipole ones of hybrid mode. With the repressing of dipole resonant mode, the increasing of transmission leads to the emergence of peak III. To further figure out the underlying mechanism, the electromagnetically induced transparency-like (EIT-like) Fano phenomenon at peak I [marked by the gray region in Fig. 3(a)] caused by the asymmetric structures is described by the coupled Lorentz oscillator model [28],

$$\begin{aligned} \ddot{x}_1 + \gamma_1 \dot{x}_1 + \omega_0^2 x_1 + \kappa x_2 &= E, \\ \ddot{x}_2 + \gamma_2 \ddot{x}_2 + (\omega_0 + \delta)^2 x_2 + \kappa x_1 &= 0, \end{aligned} \tag{1}$$

where x_1 and x_2 represent the resonant amplitude of the bright and dark modes, and γ_1 and γ_2 the corresponding damping of two modes. δ denotes the detuning of the resonant frequency of dark mode oscillator from that of the bright mode. κ stands for the coupling coefficient between the two oscillators. By fitting the experimental data, the dependence of corresponding parameters related with mode coupling on water content from 0% to 100% has been extracted and is shown in Fig. 3(d). Both the dampings of radiative and nonradiative modes represented as γ_1 and γ_2 are affected by water. More directly, based on the observation of the coupling coefficient κ decreasing from 3.49 to 2.19 THz^2, it is inferred that water may influence the average permittivity of liquid; thereby, the changed interaction in near fields reduces the resonant mode coupling of SRRs, leading to the shift of resonant frequencies and change of transmission intensity. In addition, the electric field of MMs in near fields is monitored at three resonant peaks with the thickness of water layer of 0.2 and 1 μm, respectively. As observed in Fig. 3(e), a thicker water layer generates a greater damping of THz waves; hence, the strength of localized field at MMs surface is weakened. Consequently, the transmission of THz waves would be reduced with water content increasing.

3. WAVELET TRANSFORM THEORY AND JOINT TIME-FREQUENCY ANALYSIS

From another comprehensive perspective, the coupling of the damping effect of the depletion layer with the resonating response of meta-atoms can be further revealed by using continuous wavelet transforms (CWTs),

$$W\psi f(a,b) = \langle f(t), \psi_{a,b}(t) \rangle. \tag{2}$$

It can be interpreted as the projection of $f(t)$ on the function of $\psi_{a,b}(t)$, where a is the scale parameter and b the position parameter. In our study, the complex Morlet wavelet is selected as the mother-wavelet function to process the time signals [29],

$$\psi(t) = \frac{1}{\sqrt{\pi f_b}} \cdot e^{j2\pi f_c t - (t^2/f_b)}, \tag{3}$$

where f_c and f_b are the central frequency and the bandwidth of the Morlet wavelet, respectively. If the time signal measured from THz-time domain spectroscopy (TDS) is served as $f(t)$, by using Eqs. (2) and (3), joint time-frequency analysis can be achieved, in which the parameter a is analogous to frequency and b to the temporal position. Based on this method, joint time-frequency analysis on samples is developed. Different from common fast Fourier transform (FFT), CWT not only acquires the position of resonant frequencies in a spectrum; it also tells when these resonances emerge in the time domain. In other words, the frequency spectrum given by the FFT reflects only the one-dimensional information of CWT

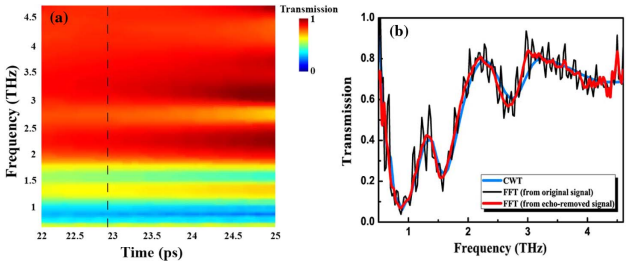

Fig. 5. (a) Time-frequency joint analysis of MIMs transmission with IPA solution flowing through; (b) comparison of frequency spectrum obtained from CWT and FFT.

results at a special temporal point. Satisfactorily, by processing the time-domain signals, the transmission in frequency domain performed by CWT agrees well with that by FFT (shown in Fig. 5), demonstrating the validity of our CWT method for the analysis.

Figures 6(a)–6(d) give the mapping of extinction intensity on time-frequency domain for water contents of 0%, 20%, 60%, and 100% in IPA liquid, respectively. Here, the extinction intensity is acquired by subtracting the transmission of the reference sample from that of the MIMs. It can be found that the MIMs platform mainly interacts with incident THz waves at two temporal points in all cases. At the time ~22 ps [indicated in Fig. 6(a) as position 1], the first interaction occurs with a relatively strong intensity, whereas the second weak interaction appears at ~34 ps (position 2). Particularly, with the enhancement of water content from 0% to 100%, two changes take place at the above positions. First, the duration Δt between positions 1 and 2 at 2.21 THz decreases from 11.74 to 11.26 ps. The underlying mechanism is that the water

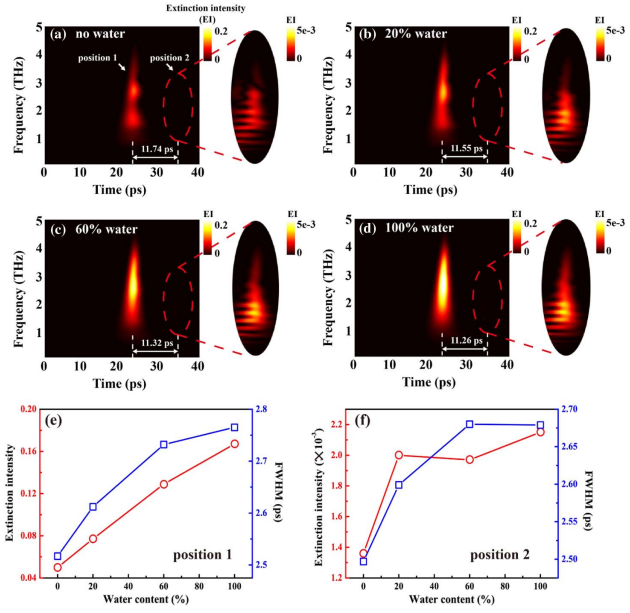

Fig. 6. (a)–(d) Joint time-frequency analysis of experimental extinction obtained from CWT at water content of (a) 0%, (b) 20%, (c) 60%, and (d) 100%. (e), (f) The dependences of extinction intensity and FWHM of Gaussian curve acquired at 2.21 THz on water content at (e) position 1 and (f) position 2 that have been marked in (a).

leads to a change in refractive index, which influences the optical path, forms the phase difference, and causes the variation of Δt in the time domain [30]. Such reduction in Δt indicates a smaller moment of inertia [31,32], implying a much easier establishment of orientation polarization. As a result, the shortened relaxation time of the depletion layer related with fast optical switching may be realized (the typical relaxation time of water has been reported by other researchers) [33,34]. Second, it is also observed that the dependence of extinction on the time domain at the frequency of 2.21 THz exhibits the Gaussian curve relation around the two positions. The corresponding peak intensity and the full width at half-maximum (FWHM) vary with the water content. As seen in Figs. 6(e) and 6(f), the extinction at positions 1 and 2 increases from 0.05 to 0.17, and from 1.4×10^{-3} to 2.2×10^{-3}, respectively. Additionally, the FWHM broadens from 2.5 to 2.8 ps for position 1 and from 2.5 to 2.7 ps for position 2. These observations from the curve also agree with the aforementioned simulation results (i.e., the strengthened damping effect induced by the molecular polarity of water in the depletion layer would produce a larger energy loss). That is why the effective modulation of transmitted THz waves can be realized by tuning the aqueous organic liquids in MIMs.

4. MODULATION PERFORMANCE OF MIMS PLATFORM

After confirming the feasibility of the proposed MIMs platform for active THz photonics, the THz modulation performance of MIMs by tuning the damping effect of the depletion layer is extensively investigated. The transmission intensity and phase shift of THz waves are measured for the MIMs with different background matrices. Figures 7(a)–7(c) present the transmission intensity mapping against water content from 0% to 100% and frequency range from 1 to 4.5 THz in three different organic liquids, respectively. As denoted in the graphs, the peak II in three cases exhibits a redshift in frequency. At the same time, with the increasing dilution of organic liquids, the transmission at the three peaks [denoted as above Fig. 3(b)] varies prominently, suggesting a high modulation efficiency for THz waves. The modulation performance of the MIMs platform is highly reliable and stable, which can also be verified in our repeatability tests (corresponding data may be requested from the authors). Moreover, not only is the transmission intensity tuned, from Figs. 7(d)–7(f), but the phase shift of THz waves also makes a significant change. By differentiating the phase shift from the frequency, the resultant group delays are acquired and show a good tunability of slow-light effect with the enhancing dilution of organic liquids [shown in Figs. 7(g)–7(i)]. Especially in IPA liquid, the peak of group delays up to 1.9 ps (only including the propagation in meta-atoms) experiences a large redshift as high as 212 GHz. In addition, the transmission and phase shift at different peaks for three organic liquids are extracted, as seen in Figs. 7(j)–7(l). The results indicate that apart from IPA, the ethanol and acetone are also good candidates as background matrices for THz waves modulation. For the three cases, the largest variation is all exhibited at peak III. For the IPA solution, the transmission intensity of peak III decreases from 84% to 14%;

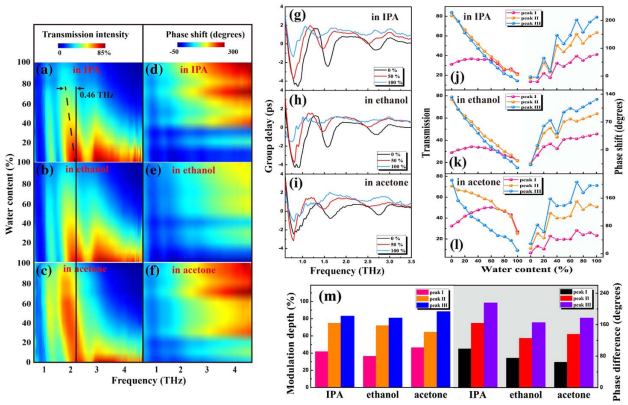

Fig. 7. (a)–(c) Dependence of measured transmission on frequency and water content in (a) IPA, (b) ethanol, and (c) acetone. (d)–(f) Dependence of measured phase shift on frequency and water content in (d) IPA, (e) ethanol, and (f) acetone. (g)–(i) Group delays under different water contents in (g) IPA, (h) ethanol, and (i) acetone. (j)–(l) Corresponding transmission and phase shift of three peaks labeled as peaks I, II, and III [as shown in Fig. 2(b)] at different water contents in (j) IPA, (k) ethanol, and (l) acetone. (m) Histogram of modulation depth and phase difference of peaks I, II, and III in different organic liquids.

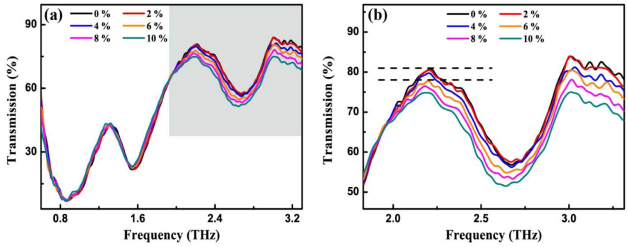

Fig. 8. Trace determination of water in IPA solution by using MIMs platforms. (a) Measured transmission of MIMs platform under the trace of water percentage increasing from 0% to 10%. (b) Enlarged version of gray region in (a); the difference of transmission is marked by dark dashed lines.

for ethanol, it reduces from 79% to 15%; and for acetone, from 76% to 9%. On the other hand, the phase shift φ (defined as $\varphi = \varphi_{sam} - \varphi_{ref}$, where φ_{sam} and φ_{ref} are the phase of MIMs and referenced sample, respectively) at peak III increases from −3° to 211° for IPA, −38° to 127° for ethanol, and 29° to 196° for acetone, respectively. It should be mentioned that the dependences of phase shift on water content roughly keep a quasi-linear relationship except for a little fluctuation. Related theoretical analysis has indicated that the amplitude of phase fluctuation is mainly caused by the amplitude of the frequency-difference fluctuation and the time difference between measurement and reference beams, and the phase fluctuation is inevitable in high-precision measurement [35]. Further, the transmission modulation depth $\Delta T/T_{max}$ of MIMs ($\Delta T \equiv T_{max} - T_{min}$, where T_{max} and T_{min} are the maximum and minimum transmission of a THz wave at different water contents, respectively) and the phase difference $\Delta\varphi$ ($\Delta\varphi \equiv \varphi_{max} - \varphi_{min}$, where φ_{max} and φ_{min} are the maximum and minimum phase shift of a THz wave at different water contents, respectively) of the three peaks for different organic liquids are shown in Fig. 7(m). It is found that the higher the frequency of the resonant peak reaches, the stronger modulation of MIMs is generated. A possible explanation is that the localized field at a higher frequency is more sensitive to the dielectric environment change due to the mode coupling. Consequently, any change in the local field turns out to result in a greater variation in transmitted THz waves. As shown in the diagrams, the largest modulation depth is always reachable at the peak III of MIMs for the three organic liquids, which is 83% for IPA, 81% for ethanol, and 88% for acetone, respectively. Meanwhile, the phase difference $\Delta\varphi$ also achieves the maximum at peak III, ~215° for IPA, 165° for ethanol, and 177° for acetone, respectively. Interestingly, the proposed MIMs platform may be of potential use in detecting residual water contents in various chemical or medical solutions. For example, as seen in Figs. 8(a) and 8(b), in the trace determination of water in IPA solution, the detection limit approaches as low as 6%, which means an augmentation of 60 μL water in 1 mL of IPA can still be sensed by the MIMs platform. This property largely spreads its functionality into a wide stage, especially in biological fields.

5. CONCLUSIONS

In summary, a novel effective technique for active modulation of THz waves is realized by engineering a depletion layer served by the aqueous organic liquid, which is flowing in a specifically designed platform of MIMs. The simulations, agreeing well with the experiments, indicate a damping effect of the depletion layer and a change of mode coupling in meta-atoms. The wavelet transform reveals an enhancement of extinction and the shortened duration in Δt with increasing dilution of an organic liquid. Meanwhile, a smaller moment of inertia indicates a much easier establishment of orientation polarization, implying a shortened relaxation time of the depletion layer. By independently coupling the damping effect of aqueous organic liquids with the resonating response of meta-atoms, the MIMs platform acquires a large modulation depth close to 90% in transmission intensity. A great phase difference over 210° is obtained in phase shift as well. This work offers a novel alternative for the active modulation of THz waves, offering new possibilities for feasible THz modulators with the introduction of an aqueous depletion layer. Moreover, it should be noted that since the THz emission from liquid water has been reported [36,37], our study may be complementary to these works, contributing to future construction of liquid-based THz systems.

Funding. National Natural Science Foundation of China (61701434, 61735010); Natural Science Foundation of Shandong Province (ZR2017MF005, ZR2018LF001); National Key Research and Development Program of China (2017YFA0700202); Programme of Independent and Achievement Transformation Plan for Zaozhuang (2016GH19); Open Fund of Key Laboratory of Opto-Electronics Information Technology, Ministry of Education (Tianjin University).

†These authors contributed equally to this work.

REFERENCES

1. D. R. Smith, J. B. Pendry, and M. C. K. Wiltshire, "Metamaterials and negative refractive index," Science **305**, 788–792 (2004).
2. W. J. Padilla, A. J. Taylor, C. Highstrete, M. Lee, and R. D. Averitt, "Dynamical electric and magnetic metamaterial response at terahertz frequencies," Phys. Rev. Lett. **96**, 107401 (2006).
3. N. Yu, P. Genevet, M. A. Kats, F. Aieta, J. Tetienne, F. Capasso, and Z. Gaburro, "Light propagation with phase discontinuities: generalized laws of reflection and refraction," Science **334**, 333–337 (2011).
4. J. D. Binion, E. Lier, T. H. Hand, Z. H. Jiang, and D. H. Werner, "A metamaterial-enabled design enhancing decades-old short backfire antenna technology for space applications," Nat. Commun. **10**, 108 (2019).
5. K. V. Sreekanth, Y. Alapan, M. ElKabbash, E. Ilker, M. Hinczewski, U. A. Gurkan, A. D. Luca, and G. Strangi, "Extreme sensitivity biosensing platform based on hyperbolic metamaterials," Nat. Mater. **15**, 621–627 (2016).
6. X. Yan, M. Yang, Z. Zhang, L. Liang, D. Wei, M. Wang, M. Zhang, T. Wang, L. Liu, J. Xie, and J. Yao, "The terahertz electromagnetically induced transparency-like metamaterials for sensitive biosensors in the detection of cancer cells," Biosens. Bioelectron. **126**, 485–492 (2019).
7. Y. Chen, X. Yang, and J. Gao, "Spin-controlled wavefront shaping with plasmonic chiral geometric metasurfaces," Light Sci. Appl. **7**, 84 (2018).
8. G. Zheng, H. Mühlenbernd, M. Kenney, G. Li, T. Zentgraf, and S. Zhang, "Metasurface holograms reaching 80% efficiency," Nat. Nanotechnol. **10**, 308–312 (2015).
9. B. Dong, X. Chen, F. Zhou, C. Wang, H. F. Zhang, and C. Sun, "Gigahertz all-optical modulation using reconfigurable nanophotonic metamolecules," Nano Lett. **16**, 7690–7695 (2016).
10. Z. Wu, X. Chen, M. Wang, J. Dong, and Y. Zheng, "High-performance ultrathin active chiral metamaterials," ACS Nano **12**, 5030–5041 (2018).
11. M. C. Sherrott, P. W. C. Hon, K. T. Fountaine, J. C. Garcia, S. M. Ponti, V. W. Brar, L. A. Sweatlock, and H. A. Atwater, "Experimental demonstration of >230° phase modulation in gate-tunable graphene–gold reconfigurable mid-infrared metasurfaces," Nano Lett. **17**, 3027–3034 (2017).
12. A. V. Diebold, M. F. Imani, T. Sleasman, and D. R. Smith, "Phaseless coherent and incoherent microwave ghost imaging with dynamic metasurface apertures," Optica **5**, 1529–1541 (2018).
13. L. Li, T. J. Cui, W. Ji, S. Liu, J. Ding, X. Wan, Y. B. Li, M. Jiang, C.-W. Qiu, and S. Zhang, "Electromagnetic reprogrammable coding-metasurface holograms," Nat. Commun. **8**, 197 (2017).
14. O. V. Dobrovolskiy, M. Huth, and V. A. Shklovskij, "Alternating current-driven microwave loss modulation in a fluxonic metamaterial," Appl. Phys. Lett. **107**, 162603 (2015).
15. T. J. Cui, M. Q. Qi, X. Wan, J. Zhao, and Q. Cheng, "Coding metamaterials, digital metamaterials and programmable metamaterials," Light Sci. Appl. **3**, e218 (2014).
16. M. Tonouchi, "Cutting-edge terahertz technology," Nat. Photonics **1**, 97–105 (2007).
17. L. Valzania, P. Zolliker, and E. Hack, "Coherent reconstruction of a textile and a hidden object with terahertz radiation," Optica **6**, 518–523 (2019).
18. W. X. Lim, M. Manjappa, Y. K. Srivastava, L. Cong, A. Kumar, K. F. MacDonald, and R. Singh, "Ultrafast all-optical switching of germanium-based flexible metaphotonic devices," Adv. Mater. **30**, 1705331 (2018).
19. M. Manjappa, Y. K. Srivastava, A. Solanki, A. Kumar, T. C. Sum, and R. Singh, "Hybrid lead halide perovskites for ultrasensitive photoactive switching in terahertz metamaterial devices," Adv. Mater. **29**, 1605881 (2017).
20. H.-T. Chen, J. F. O'Hara, A. K. Azad, A. J. Taylor, R. D. Averitt, D. B. Shrekenhamer, and W. J. Padilla, "Experimental demonstration of frequency-agile terahertz metamaterials," Nat. Photonics **2**, 295–298 (2008).
21. Y. Zhao, Y. Zhang, Q. Shi, S. Liang, W. Huang, W. Kou, and Z. Yang, "Dynamic photoinduced controlling of the large phase shift of terahertz waves via vanadium dioxide coupling nanostructures," ACS Photon. **5**, 3040–3050 (2018).
22. T.-T. Kim, H.-D. Kim, R. Zhao, S. S. Oh, T. Ha, D. S. Chung, Y. H. Lee, B. Min, and S. Zhang, "Electrically tunable slow light using graphene metamaterials," ACS Photon. **5**, 1800–1807 (2018).
23. L. Ju, B. Geng, J. Horng, C. Girit, M. Martin, Z. Hao, H. A. Bechtel, X. Liang, A. Zettl, Y. R. Shen, and F. Wang, "Graphene plasmonics for tunable terahertz metamaterials," Nat. Nanotechnol. **6**, 630–634 (2011).
24. C. A. Baron, M. Egilmez, C. J. E. Straatsma, K. H. Chow, J. Jung, and A. Y. Elezzabi, "The effect of a semiconductor-metal interface on localized terahertz plasmons," Appl. Phys. Lett. **98**, 111106 (2011).
25. K. Han, J. H. Kim, and G. Bahl, "High-throughput sensing of freely flowing particles with optomechanofluidics," Optica **3**, 585–591 (2016).
26. Y. Hu, S. Rao, S. Wu, P. Wei, W. Qiu, D. Wu, B. Xu, J. Ni, L. Yang, J. Li, J. Chu, and K. Sugioka, "All-glass 3D optofluidic microchip with built-in tunable microlens fabricated by femtosecond laser-assisted etching," Adv. Opt. Mater. **6**, 1701299 (2018).
27. H. A. Rizk and I. M. Elanwa, "Dipole moments of glycerol, isopropyl alcohol, and isobutyl alcohol," Can. J. Chem. **46**, 507–513 (1968).
28. J. Gu, R. Singh, X. Liu, X. Zhang, Y. Ma, S. Zhang, S. A. Maier, Z. Tian, A. K. Azad, H.-T. Chen, A. J. Taylor, J. Han, and W. Zhang, "Active control of electromagnetically induced transparency analogue in terahertz metamaterials," Nat. Commun. **3**, 1151 (2012).
29. A. Teolis, *Computational Signal Processing with Wavelets* (Birkhauser, 1998).
30. H. Liu, Y.-X. Fan, L. Li, H.-G. Chen, P.-F. Wang, and Z.-Y. Tao, "Self-adaptive terahertz spectroscopy from atmospheric vapor based on Hilbert–Huang transform," Opt. Express **26**, 27279–27293 (2018).
31. M. Kessler, H. Ring, R. Trambarulo, and W. Gordy, "Microwave spectra and molecular structures of methyl cyanide and methyl isocyanide," Phys. Rev. **79**, 54–56 (1950).
32. D. M. Mittleman, R. H. Jacobsen, R. Neelamani, R. G. Baraniuk, and M. C. Nuss, "Gas sensing using terahertz time-domain spectroscopy," Appl. Phys. B **67**, 379–390 (1998).
33. I. Popov, P. B. Ishai, A. Khamzin, and Y. Feldman, "The mechanism of the dielectric relaxation in water," Phys. Chem. Chem. Phys. **18**, 13941–13953 (2016).
34. P. U. Jepsen, J. K. Jensen, and U. Møller, "Characterization of aqueous alcohol solutions in bottles with THz reflection spectroscopy," Opt. Express **16**, 9318–9331 (2008).
35. J. Huang, Z. Wang, J. Gao, and B. Yu, "Modeling and analysis of phase fluctuation in a high-precision roll angle measurement based on a heterodyne interferometer," Sensors **16**, 1214 (2016).
36. Q. Jin, E. Yiwen, K. Williams, J. Dai, and X.-C. Zhang, "Observation of broadband terahertz wave generation from liquid water," Appl. Phys. Lett. **111**, 071103 (2017).
37. Q. Jin, J. Dai, E. Yiwen, and X.-C. Zhang, "Terahertz wave emission from a liquid water film under the excitation of asymmetric optical fields," Appl. Phys. Lett. **113**, 261101 (2018).